Frequency Dependent Mantle Viscoelasticity via the Complex Viscosity: cases from Antarctica and Western North America

H.C.P. Lau[1], J. Austermann[2], B.K. Holtzman[2], C. Book[1], C. Havlin[3], Emily Hopper[2], and A. J. Lloyd[2]

[1]Earth and Planetary Science, University of California, Berkeley. CA. USA.

[2]Lamont-Doherty Earth Observatory, Columbia University, NY. USA.

[3]University of Illinois, Urbana-Champaign, IL. USA.

Corresponding author: Harriet C.P. Lau (hcplau@berkeley.edu)

Key Points:

- Differing estimates of viscosity and plate thicknesses are observed from various loading processes across Antarctica and North America
- Using new theory and laboratory laws, frequency dependent viscosity and plate thickness are predicted for Antarctic and North America
- Our results indicate that these predictions of viscosity and plate thickness can significantly contribute to the observed discrepancies

Abstract

Studies of glacial isostatic adjustment (GIA) often use paleoshorelines and present-day deformation to constrain the viscosity of the mantle and the thickness of the lithosphere. However, different studies focused on similar locations have resulted in different estimates of these physical properties even when considering the same model of viscoelastic deformation. We argue that these different estimates infer apparent viscosities and apparent lithospheric thicknesses, dependent on the timescale of deformation. We use recently derived relationships between these frequency dependent apparent quantities and the underlying thermodynamic conditions to produce predictions of mantle viscosity and lithospheric thickness across a broad spectrum of geophysical timescales for three locations (Western North America, Amundsen Sea, and the Antarctic Peninsula). Our predictions require the self-consistent consideration of elastic, viscous, and transient deformation and also include non-linear steady state deformation, which have been determined by several laboratories. We demonstrate that these frequency dependent predictions of apparent lithospheric thickness and viscosity display a significant range and that they align to first order with estimates from GIA studies on different timescales. Looking forward, we suggest that observationally based studies could move towards a framework of determining the frequency trend in apparent quantities – rather than single, frequency independent values of viscosity – to gain deeper insight into the rheological behavior of Earth materials.

1 Introduction

The growth and decay of ice sheets over the Pleistocene represent large variations in Earth's climate system and induces significant deformation of Earth's solid surface and subsurface. This deformation (including associated changes to Earth's gravity field and rotation), in response to the redistribution of ice and ocean mass, is known as 'glacial isostatic adjustment' (GIA). Areas that were formerly covered by or close to major ice sheets during the last glacial period, such as North America and Antarctica, continue to experience the highest rates of GIA-related deformation, even though ice has retreated partially or entirely (e.g., Sella et al., 2007). Pertinent to understanding this solid Earth deformation (and, as a consequence, related climatological feedbacks) is knowledge of the subsurface viscoelastic structure.

The variation of GIA responses to the wide variety of mass perturbations is well studied (Nield et al., 2014; Samrat et al., 2020; Barletta et al., 2018, Ivins et al., 2011; Creveling et al., 2017; Wolstencroft et al., 2015) and analyses are often cast in terms of two controlling Earth parameters: the asthenospheric viscosity (η_{AST}) and the thickness of the lithosphere (z_{LAB}). Fig. 1 displays estimates of these two parameters from a selection of regionally overlapping geophysical studies that observed GIA responses to rapid ice sheet collapses (Barletta et al., 2018), unloading of ancient lakes (Austermann et al., 2020), glacial-interglacial scale melting (Creveling et al., 2017), and postseismic relaxation (Pollitz et al., 2000). Figs 1(a,b) reveal seemingly perplexing inconsistencies between the inferred values for these parameters even within similar study regions (see Fig. 1(c,d) for general locations, where "W-NA", "W-ANT", and "ANT-P" refer to Western North America, Western Antarctica, and Antartic Peninsula, respectively). Indeed, lateral variations in viscoelastic properties are expected as a consequence of longterm convection. Within similar locations, however, viscosity estimates from different kinds of measurements can still give rise to very different values. This apparent discrepancy can arise from two main sources: (i) differences in how the process samples interior structure; and (ii) differences in the nature – more specifically, the stress and time dependence – of the GIA response to mass perturbations (note that the studies in Fig. 1 span a wide range of timescales).

While the combination of lateral variations and subsurface sampling are significant contributors to these discrepancy (van der Waal et al., 2015; Crawford et al., 2018) and we address these issues in a first order manner, our focus here is (ii), the timescale-dependent nature of GIA. For each of these regions, by investigating predictions the frequency dependent behavior using a new theoretical framework (Lau & Holtzman, 2019) and constraints based on seismic observations and laboratory experiments, we aim to demonstrate that the consideration of timescales can also result in substantial variations in estimated values of η_{AST} and z_{LAB}. These forward predictions are independent of the GIA observations, which allows us to investigate to what extent transient rheology can reconcile estimates of η_{AST} and z_{LAB} within the three regions shown in Fig. 1.

Lateral and depth-dependent viscosity variations have been studied extensively in the literature (e.g., Hager et al., 1985; Nakada & Lambeck, 1989; Peltier, 2004; van der Wal et al., 2013; Peltier et al., 2015;). While relatively new to GIA considerations (e.g., Caron et al., 2017; Ivins et al., 2020), the timescale-dependent behavior of viscosity has long been shown in experimental studies of the mechanical behavior of rock. The endmember elastic (and anharmonic) and viscous properties of rock have been well characterized in the experimental and theoretical rock physics community (e.g., Stixrude and Lithgow-Bertelloni, 2005; Hirth and Kohlstedt, 2004). In between these endmembers is the *anelastic* or *transient* regime, which is currently being explored by several laboratories working on olivine samples (Faul and Jackson, 2015; Sundberg and Cooper, 2010) and analogue materials (Takei, 2017). This work is building towards a clearer picture of the grain-scale processes that govern macroscopic transient creep, including both diffusion- and dislocation- (both linear and non-linear) related grain boundary processes (e.g., Hansen et al., 2020). (See Havlin et al. (2020) for a summary of these processes.) From these microphysical mechanisms, distinct frequency-dependent rheological properties of rock are predicted.

In order to incorporate these frequency-dependent properties into geophysical forward predictions, they are described by phenomenological parameterizations via combinations of springs and viscous dashpots that, in isolation, characterize elastic and viscous behavior, respectively. The simplest arrangement is a single spring-dashpot pair in series, known as the Maxwell model (see Fig. 2). This is the most common viscoelastic model considered in GIA studies. Additional *transient* elements can be added to the Maxwell model to account for anelastic effects, giving rise to more complex models such as the Andrade model (Sundberg and Cooper, 2010), the Extended Burgers model (Faul and Jackson, 2015), and relaxation function fitting approaches (Takei, 2017; McCarthy et al., 2011) (Fig. 3). In addition, complexity can arise from non-linear (stress-dependent) effects (Hirth and Kohlstedt, 2004; Hansen et al., 2020). Transient behavior in form of a Burger’s rheology has been considered in some GIA studies (e.g., Caron et al., 2017) in which observations are used to constrain the two viscosities of the two distinct dashpots (Fig. 2). Comparisons between model predictions including steady-state non-linear effects and observations of deglacial sea level have also been considered in GIA (e.g. van der Wal et al., 2013; Huang et al., 2019).

In this study, we will quantify and test the role of frequency dependent viscoelastic deformation in three specific study regions (Fig. 1). In contrast to other GIA studies, we will not use GIA observations to infer the viscosity/ies of distinct dashpot/s, but instead apply the theoretical framework introduced by Lau and Holtzman (2019) to predict the continuous frequency dependent behavior for the different regions based on seismic observations and laboratory experiments. Specifically, we derive the complex viscosities, $\eta^*(\omega)$ (which is a measure of viscosity or viscous dissipation), of the viscoelastic models spanning geophysically relevant frequencies. With this approach we will treat viscoelastic rheology in a manner akin to mapping attenuation, $Q^{-1}(\omega)$, as a function of frequency within the fields of seismology and Earth tides (Shito et al., 2004; Benjamin et al., 2006; Lekic et al., 2009; Lau and Faul, 2019). In order to compare our viscosity predictions to results from prior GIA studies we first determine the frequency content of the time-domain GIA data and then test whether the predicted values of both η_{AST} and z_{LAB} as a function of frequency can explain, at least in part, some of the variation observed in these estimates.

2 Theoretical Background and Methodology

In the following, Section (2.1) will introduce the theoretical treatment of the complex viscosity and how we can use this to produce frequency dependent estimates of lithospheric thickness and asthenospheric viscosity. We will then, in (2.2), apply these ideas to the Western US and Antarctica – where the observational studies listed in Fig. 1 are located. This will consist of two parts: first, we estimate the thermodynamic subsurface structure at the selected locations and use this to determine the mechanical properties through laboratory-derived constitutive laws. We will then apply the formalism described in (2.1) to produce frequency dependent predictions of z_{LAB} and η_{AST} across these settings. Finally, in (2.3), we will turn to the observational estimates listed in Fig. 1. We will briefly summarize how they were determined and map the time-domain observationally based estimates to their distinct frequency bands. This will allow comparison between our predicted frequency trends of z_{LAB} and η_{AST} against these observations.

2.1 Rheological Background & Complex Viscosity

Lau & Holtzman (2019) introduced the complex viscosity, $\eta^*(\omega)$, parameter and its potential use in geophysical processes involving viscoelasticity. (It is more commonly used within the materials science literature, e.g., Gunasekaran & Ak, 2002.) Here we will show how $\eta^*(\omega)$ relates to more familiar parameters used in viscoelastic theory. In the time domain, for a linear viscoelastic material, one can determine the strain, ε, under small increments of stress, σ, via

$$\varepsilon(t) = \int_{-\infty}^{t} J(t - t')d\sigma(t') \qquad [1]$$

where $J(t)$ is the so-called creep function, which is the response of the material to a Heaviside function of stress (Nowick & Berry, 1972). Under different experimental conditions $J(t)$ may be determined to fit various functional forms. Equivalently, one may use the frequency domain $J^*(\omega)$, which may be found by taking the Fourier transform of $J(t)$. A closely related parameter is the complex modulus, $M^*(\omega)$, where $M^*(\omega) = [J^*(\omega)]^{-1}$ and for any of the spring-dashpot arrangements shown in Fig. 2, one may derive $M^*(\omega)$, which will have a distinct trend for any viscoelastic model.

In Fig. 2, all the viscoelastic models exhibit three regimes of deformation, partitioned by their frequency limits. The elastic regime occurs at infinite frequency limit ($f \to \infty$) where no energy is dissipated, and deformation is both instantaneous and fully recoverable. The anelastic regime, when $0 < f < \infty$, refers to deformation that remains fully recoverable but time dependent. Finally, the viscous, or steady-state regime, when $f \to 0$, wherein deformation is fully dissipative and is no longer recoverable. The total deformation is a combination of these behaviors and ultimately determined by the thermodynamic state. The spring ($f \to \infty$) and dashpot ($f \to 0$) that bookend this range of behavior involve the unrelaxed modulus, M_∞, associated with the isolated spring in series and at zero frequency, the steady state isolated dashpot in series, η_0. (The subscripts denote their frequency limit.) These purely elastic and viscous limits are relatively well agreed upon (e.g., Stixrude & Lithgow-Bertelloni, 2005; Hirth & Kohlstedt, 2004; Hansen et al., 2011) but in between, the transient/anelastic elements are less so with many combinations suggested. Determining the trajectory of rheological behavior between these endmembers, i.e., determining $M^*(0 < \omega < \infty)$, remains a goal of many laboratory studies (for review, see Faul & Jackson, 2015; Takei, 2017) but has also been explored in geophysical observations which we discuss next.

The $\mathrm{Re}[M^*(\omega)]$ reduces with decreasing frequency, causing dispersion, while $\mathrm{Im}[M^*(\omega)]$ captures the dissipative effects. Within seismology, dispersion manifests as the reduction of seismic wave-speeds at lower frequencies (e.g., Kanamori & Anderson, 1977). Similarly, attenuation, $Q^{-1}(\omega) = \mathrm{Im}[M^*(\omega)]/\mathrm{Re}[M^*(\omega)]$, increases with lower frequency (e.g., across the seismic band: Shito et al., 2004, Lekić et al., 2009; across the seismic and geodetic band:

Benjamin et al., 2006; Lau & Faul, 2019). In Fig. 3(a) we show a schematic figure of how $\mathrm{Re}[M^*(\omega)]$ and $Q^{-1}(\omega)$ are sampled by seismic waves of different frequency.

We hope to extend this analogy to GIA studies, by using a more appropriate parameter, η^*. The relationship between $\eta^*(\omega)$ and $M^*(\omega)$ is

$$\eta^*(\omega) = -i\,\frac{M^*(\omega)}{\omega},$$

and upon inspection, one can see that η^* has the same units as viscosity, where the real and imaginary parts have now been switched relative to M^*. No matter the arrangement of springs and dashpots (Fig. 2), just as with M^*, a continuous function across frequency may be derived for η^*. Just as the dispersion of wave-speed captures $\mathrm{Re}[M^*(\omega)]$, we argue that estimated viscosities determined by different observations are sampling $\|\eta^*(\omega)\|$ at their respective frequency bands (Fig. 3b), where we have plotted $\|\eta^*(\omega)\|$ of a Maxwell viscoelastic model. This trend may be interpreted as an indication of the degree of viscous dissipation at a given forcing frequency (Lau & Holtzman, 2019).

Assuming we have determined the continuous form of $\eta^*(\omega)$ given an appropriate viscoelastic model (Fig. 2), we introduce two simple parameters, the *apparent viscosity*, $\tilde{\eta}(\omega)$ and the *apparent lithospheric thickness* $\tilde{z}_{\mathrm{LAB}}(\omega)$, where the former is simply

$$\tilde{\eta}^*(\omega) \equiv \|\eta^*(\omega)\| = \sqrt{\mathrm{Re}[\eta^*(\omega)]^2 + \mathrm{Im}[\eta^*(\omega)]^2}.$$

The conceptual step we have taken in this study is to *reinterpret* what the studies collated in Fig. 1 termed η (or more specifically, as they applied Maxwell models, η_0) as apparent viscosity $\tilde{\eta}(\omega_{\mathrm{obs}})$, where ω_{obs} is the frequency of observation (in practicality, this is a frequency band, Section 2.3). In the same vein, we interpret LAB depths as *apparent lithospheric thickness* or *apparent LAB depths*, $\tilde{z}_{\mathrm{LAB}}(\omega_{\mathrm{obs}})$. This parameter is explored in greater detail in Lau et al. (2020) and we only briefly describe the method by which we determine $\tilde{z}_{\mathrm{LAB}}$ below.

First, we define the Maxwell time, τ_{M}, of any viscoelastic media as η_0/M_∞. Thus, considering only depth (z) dependent variation in structure, we have $\tau_{\mathrm{M}}(z)$. If we are interested in z_{LAB} at a given frequency, e.g., 1/1000 y^{-1}, we find the depth at which the value of τ_{M}^{-1} is equivalent to 1000^{-1} y^{-1}. This essentially marks the transition from elastic to viscous behavior at a given frequency. This definition breaks down at frequencies higher than the Maxwell frequency, where we propose that z_{LAB} becomes essentially frequency independent. At these high frequencies, the notion of a plate itself becomes unclear. We note that this is just one definition of many that exist for the LAB, though this definition highlights the frequency dependence of z_{LAB}.

2.2 Predicting of Apparent Lithospheric Thickness and Asthenospheric Viscosity in Anarctica and western North America

We focus on three regions matching those in Fig. 1: Western North America (W-NA), Western Antarctica (W-ANT), and the Antarctic Peninsula (ANT-P). For each location we determine depth dependent profiles of upper mantle mechanical properties across the full spectrum in frequency relevant to geophysical timescales. This includes implementing elastic, anelastic, and viscous constitutive laws in a self-consistent manner, using the recently released software library known as the "Very Broadband Rheology" (VBR) calculator (https://vbr-calc.github.io/vbr/; Havlin et al., 2020). This software library takes thermodynamic conditions and a chosen composition as input and applies chosen constitutive laws to predict $M^*(\omega)$. From $M^*(\omega)$ we may extract $\tilde{z}_{\mathrm{LAB}}(\omega)$ and $\tilde{\eta}_{\mathrm{AST}}(\omega)$. Hereafter, we use the term *combined constitutive laws* when referring to the full-spectrum constitutive law which ties together elastic, anelastic and viscous constitutive laws and for all the figures and calculations within the main text, we use the laws of Stixrude & Lithgow-Bertelloni (2005), MacCarthy et al. (2011), and Hirth & Kohlstedt (2004), respectively. We explore how our predictions change when different anelastic laws are applied in the Supporting Information.

The self-consistency in the combined constitutive law is important to explain: The individual constitutive laws (multiple sets for elastic, viscous and anelastic) are derived from different laboratories, which have different scalings from laboratory- to earth-conditions and are all implemented within the VBR calculator, to facilitate comparison. Different anelastic models incorporate the elastic and viscous laws differently (Havlin et al., 2020), leading to different degrees of self-consistency in the combined constitutive laws, a topic beyond the scope of this paper. In this paper, we use one combined constitutive law to infer thermodynamic state from measurements made in the seismic band and then use that same law to extrapolate across the entire geophysical spectrum to predict wideband mechanical behavior. Thus, our first step is to determine the thermodynamic conditions (temperature and pressure, T and P, respectively) beneath these regions. The entire workflow is summarized in Fig. 4.

2.2.1 Determining the Thermodynamic Conditions

To estimate the subsurface thermodynamic structure, **S**, beneath each of our regions, we approximated each by a simple plate model characterized by a conductive lid of thickness z_{LID}, above which heat is lost via conduction and beneath which the temperature follows that of an adiabat characterized by a potential temperature T_{P}. (Note that z_{LID} is not necessarily equivalent to z_{LAB} depending on the definition used by the different studies we include.) This estimation occurs in two steps.

First, we used seismic tomographic models to extract the observed asthenospheric shear wave-speed, v_{S}, for each region: Shen & Ritzwoller (2016) for W-NA and Lloyd et al. (2020) for all of Antarctica. For each region, we extracted a single v_{S} value by horizontally averaging over a radius of 50 km surrounding the stars (Figs 1(c,d)) and vertically averaging between the shaded orange shaded region (Figs 5a-c, subpanels i-ii), a region encapsulating the asthenosphere just beneath the plate. (We note that we tested the lateral averaging affects by repeating the calculations over radii spanning 50-200 km and our conclusions remain the same, though this length-scale may be regionally dependent (e.g., Lau et al., 2018).) Using this tomographic v_{S} value (see circle in Figs 5a, subpanels i) at its reported seismic band (see each reference), we determined the temperature at the associated depth by using the VBR calculator. For this purpose, the VBR maps state variables **S** to mechanical properties (e.g., v_{S} at the appropriate frequency), and then using Bayesian inference, finds the best fitting set of state variables given the seismic input from tomography (Havlin et al., 2020). Extrapolating the temperature value along the adiabatic gradient to the surface provides us with the associated T_{P} (Havlin et al., 2020). The simplification of characterizing each region as a plate model means that both T_{P} along with the adiabatic gradient are sufficient to describe the asthenospheric thermal profile for each region. The smoothness of the v_s profiles from these tomography models (Fig. 5, subpanels i) suggests that such an approximation is reasonable for these regions.

With the asthenospheric thermal profile constrained for each region, we then create a suite of plate profiles, $\mathbf{P}_i$ (where $i = 1, 2, ..N$), where each i-th profile requires the following parameters as input: homogenous grain size g_i, melt fraction ϕ_i, water content X_{H2O}, and major composition X_{maj}. Each profile $\mathbf{P}_i$ is determined by solving the 1-D transient heat equation with a conductive lid until steady state is reached for a given i-th set of parameters. To produce N profiles, we vary the following parameters: g = [0.001, 0.004, .., 0.03] m, and ϕ = [0., 0.005, .., 0.03]; while holding the compositions constant, i.e., X_{H2O}= 0, X_{maj} = olivine (90% forsterite). We also then vary the thickness of the conductive lid, between [50, 60, …, 250] km. Thus far, this procedure is shown by steps (1) and (2) in Fig. 4.

In the second step, we set out to determine the plate profile with the best fitting z_{LID} (step (3) in Fig. 5). We use observed values of LAB depths, or $z_{\mathrm{LAB}}^{\mathrm{obs}}$, derived from the seismic studies of Hopper & Fischer (2018) for W-NA and An et al. (2015) for all of Antarctica. We treated each differently as $z_{\mathrm{LAB}}^{\mathrm{obs}}$ has different definitions within the two models. (The definition of the lithosphere is not universal, as discussed in detail by Lau et al. (2020) and further provides motivation for the notion of *apparent plate thickness*.). We reproduced each study's version of $z_{\mathrm{LAB}}^{\mathrm{obs}}$ from our N plate models. For the Antarctic lithospheric model, $z_{\mathrm{LAB}}^{\mathrm{obs}}$ coincides with the intersection of the base of the conductive plate and the adiabatic gradient (estimated from seismic data), and thus, z_{LID}, which we impose for each $\mathbf{P}_i$, and $z_{\mathrm{LAB}}^{\mathrm{obs}}$ are the same. For W-NA, Hopper & Fischer (2018) define the LAB as the most negative $\partial v_{\mathrm{S}}/\partial z$ value. Hence, for W-NA, for our suite of $\mathbf{P}$, the VBR calculator predicted the v_{S} profile at the appropriate seismic frequency bands using the combined constitutive laws from which we extract $\partial v_{\mathrm{S}}/\partial z$ and find the depth at which this value is most negative.

With these LAB constraints we use Bayesian inference (see Havlin et al., 2020, for more details) to produce posterior probability distributions of the thickness of the conductive lid and each state variable we vary. We assumed that prior knowledge for each state variable is represented by a uniform probability density function over the ranges we have stated. We ascribe a uniform uncertainty distribution of ±5% and ±5 km for the observed v_S and $z_{\mathrm{LAB}}^{\mathrm{obs}}$. As a result, for each region, we select the model with the highest joint probability distribution. The best fitting v_s profiles are shown in Figs 5(a-c), subpanels (ii). For reference, in Figs 5(a-c), subpanels (ii), the circles mark the v_s values of the resulting best fitting models within the depth range that they were required to fit the observed profiles (shaded region). The corresponding temperature profiles, determined by a combination of assuming an adiabatic gradient and thickness of the conductive lid, are shown in Figs. 5(a-c), subpanels (iii) (black lines). In Fig. S1 we show the resulting joint probability distributions for each region, highlighting the trade-offs between various parameters.

2.2.2 Determining apparent viscosity and apparent lithospheric thickness

Having identified the best fitting thermodynamic conditions, i.e., $\mathbf{S}_{i=\mathrm{best}}$, for each region, we used the VBR calculator with this input to predict several mechanical parameters using the combined constitutive law, including the complex modulus ($M^*(z,\omega)$), complex viscosity ($\eta^*(z,\omega)$), and attenuation $Q^{-1}(z,\omega)$ (shown in Fig. S2). This corresponds to step (4) in the flowchart (Fig. 4).

From Section 2.1 it is now straightforward to see how, from $M^*(z,\omega)$, one can extract $\tilde{\eta}_{\mathrm{AST}}(\omega)$ and $\tilde{z}_{\mathrm{LAB}}$. In order to do this, we determine η^* from M^*, and the results of these predictions are shown in Figs 5(a-c), subpanels (iii-v). For the anelastic regime, where more uncertainty exists across different constitutive laws, we applied several other laws shown in Fig. S3 to explore this uncertainty (analogous to results of Fig. 5, using experimental laws of Faul & Jackson (2015) and the premelting model of Yamauchi and Takei (2016) (see also Takei, 2017).

2.3 Determining the Frequency Content of Observationally Derived $\tilde{\eta}_{\mathrm{AST}}$ and $\tilde{z}_{\mathrm{LAB}}$

Observationally derived estimates of lithospheric thickness and viscosity are generally obtained by combining knowledge of past load changes (ice sheets or lakes) with observations of deformation (GPS or reconstructions of paleo-water level) assuming a viscoelastic model. The estimates we have used for comparison against our VBR-driven profiles are all parameters reported from studies with various observational constraints (mostly geodetic and geologic), and thus are subject to a range of simplifying assumptions. The estimates of both z_{LAB} and η_{AST} have been compiled from the following investigations for each region (listed in order of decreasing timescale): For Western North America, estimates were derived from paleo sea-level indicators that measure GIA during Marine Isotope Stages 5a and 5c (~80 and ~100 ky BP, respectively) (Creveling et al., 2017), paleo-shorelines recording rebound at Lake Bonneville and Lake Provo (~14 ky BP) (Austermann et al., 2020), and geodetic observations of postseismic relaxation after the 1992 Landers earthquake (Pollitz et al., 2000). In addition, we included the z_{LAB} estimate inferred from GPS estimates of the postseismic relaxation following the 2010 El Mayor-Cucapah earthquake (Dickinson-Lovell et al., 2018). For Western Antarctica, Barletta et al. (2018) used GPS derived measures of decadal-scale rebound at the Amundsen Sea Embayment. Finally, for the Antarctic Peninsula, decadal (Nield et al., 2014; Samrat et al., 2020) and centennial (Ivins et al., 2011; Wolstencroft et al., 2015) responses to ice mass change, once more, measured by GPS, were used to derive viscosity estimates.

These studies result in different estimates of z_{LAB} and η (Fig. 1) and as described in the Introduction, these variations may in part arise from the differing thermodynamic conditions of the subsurface structure and how the GIA process samples this. In the most ideal scenario we would consider only observations that sample exactly the same earth structure, but only on different timescales. In reality, these kind of observations do not yet exist and we can only minimize the effect of sampling different earth structure. To do this, we have chosen to focus on studies that cover similar geographic regions and mostly sample the asthenosphere.

In order to compare our predictions of $\tilde{\eta}_{\mathrm{AST}}(\omega)$ and $\tilde{z}_{\mathrm{LAB}}(\omega)$ to the observations presented in Fig. 1, we first reinterpreted these viscosities and lithospheric thicknesses as *apparent* quantities. Next, we must determine their frequency content, which requires us to consider two important timescales associated with each observation: τ_{dur}, the duration over which the loading/unloading event in question occurred, and τ_{del}, the time delay between the end of the event and when the observation of solid Earth deformation was taken. For example, z_{LAB} and η estimates from the the loading of Lake Bonneville (Austermann et al., 2020) occurred across a timespan ~4,000 y

($\tau_{\mathrm{dur}}\sim$ 4,000 y), and measurements of rebound are recorded as dated shorelines during the loading period, and as such, we assign $\tau_{\mathrm{del}}\sim$ 0 y. (We note that the long-term GIA deformation associated with the Laurentide ice sheet was still ongoing during the late unloading, we consider this secular deformation as background. In that study, the authors considered the two processes distinct.) These designations of τ_{del} and τ_{dur} – tabulated and briefly explained for each observation in Table S1 – are approximate but our aim is to cover a wide enough frequency band to provide the most conservative estimate possible. With these two timescales we assign each process a frequency band, $[f_{\mathrm{low}}, f_{\mathrm{upp}}]$, applying an empirical relationship based on replicating the loading history and measurement of deformation, as described below.

In Section 2.1 we introduced how the creep function, J, relates the strain of a material to an applied stress (Eq. 1). In order to replicate a generic loading history and measurement of deformation, we apply the stress history shown in Fig. 6(a), where we have schematically depicted the timespans of τ_{dur} and τ_{del}. In order to estimate the frequency content within this deformation response, we require knowledge of $J(t)$ and $J^*(\omega)$. This is not always straightforward (e.g., Nowick & Berry, 1972) and so we turn to the 1-D Andrade model, J_{An} (Fig. 2). We choose the Andrade model since it can capture the full spectrum of viscoelastic (elastic, transient, viscous) behavior with few model parameters (Cooper, 2002) and its expression for $J^*_{\mathrm{An}}(\omega)$ is known, where

$$J_{\mathrm{An}}(t) = \frac{1 + {}^{t}/_{\tau_{\mathrm{M}}}}{M_\infty} + \beta t^n$$

and

$$J^*_{\mathrm{An}}(\omega) = J_\infty + \beta\Gamma(1+n)\omega^{-n}\cos\left(\frac{n\pi}{2}\right) - i\beta\Gamma(1+n)\omega^{-n}\sin\left(\frac{n\pi}{2}\right) + \frac{1}{\eta_0\omega}$$

(Faul and Jackson, 2015). Our aim is to use these analytical expressions to fit those that have been output by the VBR so that we can mimic loading histories for these viscoelastic models and readily move between the time and frequency domain. To do so, for all regions, we chose n as 1/3 (Cooper, 2002), used the VBR output values of τ_{M}, M_∞ associated with each region, and solved for the best fitting β value via a grid search. More specifically, we determined apparent viscosities from Andrade models with many values of β and selected the model that reproduced the apparent viscosity trends from the VBR, where Fig. 6b shows our final fits for each region.

The solid lines are reproduced from Fig. 5 (subpanels v). With the simple time domain expression for $J(t)$ we can readily perform the convolution in Eq. 1.

We apply the linearly increasing load for a period of τ_{dur} depicted in Fig. 6(a) and perform many tests across the range ($10^{-2} \leq \tau_{\mathrm{dur}} \leq 10^{6}$) years, effectively varying the stress rate, and convolve this with the best fitting $J_{\mathrm{An}}(t)$ expressions. In order to emulate measurements made by the unloading/loading scenarios in our dataset, we determine the resulting strain rate, $\dot{\varepsilon}$ from Eq. 1. We make $\dot{\varepsilon}$ values at various values of τ_{del} across the range ($10^{-4}\tau_{\mathrm{dur}} \leq \tau_{\mathrm{del}} \leq 10^{4}\tau_{\mathrm{dur}}$) years, a range that covers all scenarios. Using the strain rate, we estimate the viscosity assuming a *Maxwell viscoelastic model*, η_{est}, and that we know M_{∞} and $\sigma(t)$ (all assumptions made by the studies included here). For the simple 1-D case,

$$\eta_{\mathrm{est}} = \sigma\left(\dot{\varepsilon} - \frac{\dot{\sigma}}{M_{\infty}}\right)^{-1}.$$

As argued previously, these viscosity estimates are capturing the *apparent* viscosity of the underlying Andrade model, i.e., $\tilde{\eta}_{\mathrm{An}}$, at its respective frequency. In order to map out the frequency band for which values of η_{est} capture we first consider f_{upp}. For f_{upp} we know that, given the timescale of any process, the highest possible frequency must be bound by τ_{dur}^{-1}. The Fourier transform of a linear trend is dominated by low frequencies and longer values of τ_{del} will result in any relatively high frequency response to diminish. But just how low is this bound? For f_{low} we find the frequency for which $\tilde{\eta}_{\mathrm{An}}$ (derived from $\tilde{J}^{*}_{\mathrm{An}}(\omega)$) is equivalent to η_{est}. For each observation, we show the frequency band dictated by τ_{dur} and τ_{del} in Fig. 6(c-e).

3 Results and Discussion

3.1 Reconciling observational estimates of asthenospheric viscosity and plate thickness

Fig. 1 displays differing estimates of what studies report as measures of elastic plate thickness and Maxwell viscosity at the listed locations. These differences may be due to the variations in thermodynamic setting and/or forcing timescale dependent effects. In Fig. 5, we divide these observation-driven estimates into their respective regions and account for the broad thermodynamic conditions (to reduce the effect of the former) and recast these estimates as frequency dependent apparent viscosities (to highlight the latter). By doing this, we see that the frequency dependence of the forcing may play a substantial role. In all locations the apparent viscosity decreases as a function of increasing frequency, while $\tilde{z}_{\mathrm{LAB}}$ increases with increasing frequency. At high frequency, we find that $\tilde{z}_{\mathrm{LAB}}$ is at a maximum as one must go to hotter conditions (i.e., deeper depths) for this elastic-to-viscous transition to occur. Toward longer timescales, $\tilde{z}_{\mathrm{LAB}}$ relaxes to shallower depths (Fig. 5, subpanels (iv)).

In Fig. 5, we have also placed the apparent viscosities and plate thicknesses obtained from observational estimates (Fig. 1) in order to compare them against our modeled predictions. Across all regions some of the observations of $\tilde{\eta}_{\mathrm{AST}}$ (subpanels (iii)) fit our predicted values well (colored lines) and some fall within the shaded regions, which we discuss in the next section. A slightly less clear picture is seen with $\tilde{z}_{\mathrm{LAB}}$, where qualitative trends agree but several observations do not align with the predictions of $\tilde{z}_{\mathrm{LAB}}$ (colored lines). Where $\tilde{z}_{\mathrm{LAB}}$ observations and predictions match reasonably well are at W-ANT and W-NA (with some falling within the shaded region). Uncertainties in $\tilde{z}_{\mathrm{LAB}}$ estimates in the ANT-P region are quite large and do not overlap across the same frequency bands. For this region, it is important to consider that the continental lithosphere is comprised of a narrow peninsula rather than a large continental interior and observations made at ANT-P (which, across the studies included, span the stretch of the peninsula) may be sampling aspects of both the lithosphere beneath the narrow peninsula and the surrounding oceanic region. In addition, slightly beneath the depth range we consider, there is a subducting slab that may also affect GIA (Lloyd et al., 2020). Our simple depth dependent profiles may not sufficiently capture this complexity and/or z_{LAB} measurements are not well constrained by the type of observation used.

While lateral variations in thermodynamics and the potential variability in the sampled subsurface of each observation can contribute to the variability in z_{LAB} and η_{AST} within each region, our comparison between these observation-driven estimates and VBR determined predictions of frequency dependent parameters convincingly illustrates that such processes are not only important to consider, but can in fact explain some of the variation in GIA based estimates. We therefore suggest moving towards an estimation framework that aims to map out the continuous frequency trend of $\tilde{\eta}(\omega)$ through observations of different frequency – akin to mapping out the frequency dependence of $Q^{-1}(\omega)$ in seismic studies (Fig.3). If a complete trend may be mapped, more concrete inferences on the underlying viscoelastic model may be made. However, unlike the seismic application, quantifying the frequency content for any given time-domain GIA process is not trivial and while we propose one approach here (section 2.3), we argue that further work is required to better understand this relationship. In the next section, we discuss the deformational processes that may be responsible for these values of $\tilde{\eta}(\omega)$.

3.2 Grainscale deformation processes and their manifestation in GIA

The steady-state viscosity profiles (Fig. 5; colored bold lines, subpanels (iii)) of each region show the structure most relevant to mantle convection timescales. The horizontal-colored line shows the depth at which $\tilde{z}_{\mathrm{LAB}}$ occurs at the zero-frequency limit. This can be thought of as the *true* thickness of the plate – which, by many definitions with the literature, is the base of the top thermal boundary layer of mantle convection, above which conduction is the mode of heat loss (Fisher et al., 2010). However, as Lau et al. (2020) argue, many studies infer *apparent plate thickness* at the frequency of the unloading process (colored bold lines, subpanels (iv)). For example, changes in seismic velocity gradients, seismic anisotropy measurements, receiver functions and attenuation data (Hopper & Fischer, 2018; Mancinelli et al., 2017) have been used to infer $\tilde{z}_{\mathrm{LAB}}$ at frequencies of ~(0.01-0.1) Hz. This inference of $\tilde{z}_{\mathrm{LAB}}$ lies towards the far right of subpanels (iv) (grey bar). The physical relationship between the seismic LAB and the convective LAB is discussed in more detail in Lau et al. (2020). As can be seen, moving towards lower frequency $\tilde{z}_{\mathrm{LAB}}$ relaxes to significantly shallower depths as the asthenosphere beneath becomes increasingly viscous, impinging on the rigid plate above. These panels demonstrate that one cannot assume that LAB values inferred on seismic timescales are appropriate for processes acting on convection timescales. For example, in W-NA the LAB ranges from 75, 50, to 35 km when probed at the seismic, ice age, and convective timescales, respectively. An analogous discussion based on the *Effective Elastic Thickness* of plates at different timescales may be found in Watts et al. (2013).

Now examining $\tilde{\eta}_{\mathrm{AST}}(\omega)$ (colored bold lines, subpanels (v)), we see a significant increase towards lower frequency spanning several orders of magnitude for all regions. At the high frequency extreme, $\tilde{\eta}(\omega \to \infty)$ tends towards zero, as we move towards the purely elastic regime of deformation. Once more, the *apparent viscosity* cannot be mistaken for η_0; this latter value is reached at low frequencies, depicted by the plateau of $\tilde{\eta}(\omega)$ on the low frequency end of our plots. So, what might we infer from these results about the activation of certain deformation mechanisms?

3.2.1 Diffusion Creep

For the solid lines in Fig. 5, the underlying mechanism is diffusion creep. In GIA, the most commonly adopted viscoelastic model used to phenomenologically describe such creep is the Maxwell model (as is the case with all the observations included here). However, such a model does not capture *transient* diffusion creep, arising from stress concentrations at grain edges, driving diffusive flow of matter through grain boundaries or sub-grain boundaries, causing those stress concentrations to relax (e.g. Cooper, 2002 and references therein). This process is considered to cause the so-called *High Temperature Background* ("HTB") attenuation. Additional dissipative mechanisms that can be superposed onto the HTB in the linear anelastic regime include elastically accommodated grain boundary sliding , melt squirt, dislocation damping (at constant dislocation density), and other processes (e.g. Cooper, 2002; Havlin et al, 2020). Transient diffusion creep relaxes to steady-state, diffusionally accommodated grain boundary sliding (Cooper, 2002; Faul & Jackson, 2015). These processes can be activated at different frequencies depending on the thermodynamic state, and the associated dissipation is often parameterized within the experimental community by the intrinsic attenuation, $Q^{-1}(\omega)$ (i.e., the fractional average energy dissipated per cycle of oscillation).

Here, we can assess here the degree to which transient creep may contribute to the trend in $\tilde{\eta}(\omega)$ captured by our selected observations. The solid color lines in subpanels (iv) and (v) capture the trend of the HTB model (where, as well as the elastic and viscous endmembers, we include HTB transient diffusion only – in the case of the Main Text examples, the latter is the constitutive law of McCarthy et al. (2014)). The dashed colored lines are identical but with no transient creep component, representing a Maxwell model with the same η_0 and M_∞ values. The departure in $\tilde{\eta}$ between the full and equivalent Maxwell models clearly occurs across a frequency band spanned by most of the processes we consider. While these differences in $\tilde{\eta}$ seem slight in these figures, the ratio between these two models can be as low as ~50%, emphasized in the plots of normalized eta* in Lau et al, 2020. Our data here cannot distinguish the difference between the two trends of $\tilde{\eta}$, but future studies may be designed to identify the degree of HTB transient creep and explore additional dissipative mechanisms in such deformation.

3.2.2 Dislocation Creep

Diffusion creep rate is linear in stress and relevant at low levels of both strain and stress , where deformation *probes* the microstructure but does not modify it. Processes like GIA and seismic wave propagation are characterized by small strains (~10^{-5}) and low stresses (~kPa), such that it is possible that transient diffusion creep dominates any transient response. and likely that grain sizes are not modified by those processes. However, crystallographic fabrics of xenoliths and ubiquitous seismic anisotropy in the upper mantle implicate an important role for dislocation creep at least at convective time scales.

A non-linear transient regime may be reached in which a forcing process produces dislocations, modifying the dislocation density *during* the process and affecting the transient response (e.g., Farla et al., 2012; Cooper et al., 2016; Thieme et al., 2018). At increasing levels of stress, dislocation density increases, causing rock to weaken. If the forcing level (applied stress) is constant or changing slowly enough (quasi-static), dislocation density can be considered constant and the dislocation creep rate is steady state, as characterized by numerous laboratory studies. While full self-consistency regarding the role of dislocation creep would incorporate both the transient and the steady state roles of dislocations, such a composite constitutive model across the range of conditions of interest here does not yet exist, though much research is underway (Hansen et al., 2020).

Towards estimating the potential effects of dislocation creep in the wide-band responses considered here, we can easily incorporate steady state dislocation creep into the current framework without considering the transient role of dislocations. This extra mechanism is phenomenologically represented by an additional steady-state, stress-dependent dashpot, labeled η_{disl}, in series with the linear Maxwell steady-state dashpot, η_0 (Fig. 2). The effective steady-state stress is dominated by the dashpot with the lower viscosity. In subpanels (iii-v) of Fig. 5, shaded regions reflect the effect of steady-state dislocation creep (Hirth & Kohlstedt, 2005), and encompass variations in η_0, $\tilde{z}_{\mathrm{LAB}}$, and $\tilde{\eta}_{\mathrm{AST}}$ from stresses (σ) ranging where ($0 \leq \sigma \leq 10$) MPa (where colored bold lines and fine gray lines coincide with 0 and 1 MPa, respectively). As shown by these regions, macroscopically, there is a reduction in all parameters in Fig. 5 and the transition of $\tilde{z}_{\mathrm{LAB}}$ is shifted to higher frequency as the effective Maxwell time is now reduced. We note that, in certain parts of the plate, GIA processes reach such levels of stress (in Fig. S4 we show the deviatoric stress beneath the ice sheet over a representative GIA cycle). Since several of the observations fall within these shaded regions, it is possible that nonlinear deformation is occurring to explain these estimates of $\tilde{\eta}_{\mathrm{AST}}$ and $\tilde{z}_{\mathrm{LAB}}$.

3.3 Implications for ice mass change and sea-level change

Ice mass change, both past and present, span a wide frequency spectrum, and we show here that so too does the variation in the solid Earth's response to such perturbations. Based on our results we suggest that by reinterpreting estimates of viscosity and plate thickness as *apparent viscosities* and *apparent plate thicknesses* these seemingly diverging values may be reconciled. We also show that laboratory-based constitutive laws suggest that transient creep plays some role across the span of our observations (from rapid to ~10 ky timescales).

Ultimately, ignoring deformational mechanisms acting across the wide frequency range of GIA processes may lead to misestimation of the sea-level response, whether those include rapid ice collapse, where studies typically invoke a purely elastic Earth (e.g., Gomez et al., 2010) or solid Earth responses modeled purely as Maxwell viscoelastic solids. For example, following our results shown in Fig. 6(b), we predict that if the same amount of ice retreat in the Amundsen Sea area occurred over 1, 10, 100, and 1000 y, the asthenospheric apparent viscosity would be ~10^{18}, ~6×10^{18}, ~10^{19}, ~6×10^{19} Pa s. This may have implications for the stabilizing effect of GIA on the Antarctic ice sheet, which affects predictions of future sea level change.

A further compounding factor on all timescales is that high frequency and high magnitude melt events will result in high strain rates that may require the consideration of non-linear rheology that, as discussed previously, involves changes in the dislocation structure driven by these large external stresses. It is unclear how such extraneous stress regimes might alter GIA during these events, but one might expect that the apparent viscosity would be significantly reduced due to stress magnitude and the relatively high frequency of such intense melting events. So far non-linear rheologies have only been considered in isolation (van der Waal et al., 2013, Huang et al., 2019), but our preliminary calculations presented here show that these effects have repercussions across a wide frequency band.

4 Conclusions

The adoption of the Maxwell viscoelastic models from the early semi-analytical techniques derived (Wu & Peltier, 1982; Mitrovica & Milne, 2003) offered an elegant means to solve a complicated viscoelastic system and fit a whole range of sea-level and geodetic observations. The realization, however, that temperature effects alone result in lateral variations in viscosity that span orders of magnitude required a distinct departure from these semi-analytic techniques and a movement towards computationally demanding finite-element methods that continues today (e.g., Zhong et al., 2003; Latychev et al., 2005; van der Waal et al., 2005).

With a growing richness in datasets that capture increasingly subtle signals of ice melt, we believe the next level of complexity must be met. Our results outlined here have highlighted a potential pathway towards considering both thermodynamic variations within Earth’s subsurface and the nature of the forcing (both frequency and stress) for GIA-related processes. We have applied a means of self-consistently interpreting observational results that span the full spectrum in frequency. There are several simplifications we have made in order to focus on this full spectrum behavior: we have broadly interpreted viscosity estimates – drawn from a diverse set of studies each with their own assumptions and spatial sensitivities – as apparent viscosities of the asthenosphere, and we have considered depth dependent plate profiles for each region, neglecting lateral variations in thermodynamic environment and assuming that each region may be approximated as a plate model. (Though we emphasize that we were equally mindful of choosing observations that reflected these specific regions both geographically, and in depth.)

Nevertheless, in doing so, we have demonstrated that our current understanding of Earth deformation, derived from microphysical investigations that operate on timescales appropriate for the laboratory setting, shows significant promise in explaining much of the variability we observe on the planetary scale and across timescales that capture Earth's long and nuanced history. Looking to the future, we encourage both the inclusion of viscoelastic models in GIA that move beyond the Maxwell model (e.g, Yuen et al., 1986; Ivins et al., 2020), the determination of the frequency content within measurements of time-domain processes like GIA, and the search to map out the continuous function $\tilde{\eta}(\omega)$, rather than discrete values of η_0, to help improve predictions of cryosphere-solid Earth responses as rates of ice sheet melting and collapse increasingly occur on shorter timescales.

Acknowledgments

HL acknowledges support from UC Berkeley. All codes pertaining to this study are available within the Zenodo reference, doi:10.5281/zenodo.3738485.

References

Abe-Ouchi, A., Saito, F., Kawamura, K., Raymo, M.E., et al. (2013) Insolation-driven 100,000-year glacial cycles and hysteresis of ice-sheet volume. *Nature*. [Online] 500 (7461), 190–193. Available from: doi:10.1038/nature12374 [Accessed: 17 October 2017].

Austermann, J., Chen, C.Y., Lau, H.C.P., Maloof, A.C., et al. (2020) Constraints on mantle viscosity and Laurentide ice sheet evolution from pluvial paleolake shorelines in the western United States. *Earth and Planetary Science Letters*. [Online] 532, 116006. Available from: doi:10.1016/j.epsl.2019.116006.

Barletta, V.R., Bevis, M., Smith, B.E., Wilson, T., et al. (2018) Observed rapid bedrock uplift in amundsen sea embayment promotes ice-sheet stability. *Science*. [Online] 360 (6395), 1335–1339. Available from: doi:10.1126/science.aao1447.

Benjamin, D., Wahr, J., Ray, R.D., Egbert, G.D., et al. (2006) Constraints on mantle anelasticity from geodetic observations, and implications for the J 2 anomaly. *Geophysical Journal International*. [Online] 165 (1), 3–16. Available from: doi:10.1111/j.1365-246X.2006.02915.x [Accessed: 29 February 2016].

Caron, L., Métivier, L., Greff-Lefftz, M., Fleitout, L., et al. (2017) Inverting Glacial Isostatic Adjustment signal using Bayesian framework and two linearly relaxing rheologies. *Geophysical Journal International*. [Online] 209 (2), 1126–1147. Available from: doi:10.1093/gji/ggx083.

Conrad, C.P. & Lithgow-Bertelloni, C. (2006) Influence of continental roots and asthenosphere on plate-mantle coupling. *Geophysical Research Letters*. [Online] 33 (5), L05312. Available from: doi:10.1029/2005GL025621 [Accessed: 4 February 2016].

Cooper, R.F. (2002) Seismic Wave Attenuation: Energy Dissipation in Viscoelastic Crystalline Solids. *Reviews in Mineralogy and Geochemistry*. [Online] 51 (1), 253–290. Available from: doi:10.2138/gsrmg.51.1.253.

Cooper, R.F., Stone, D.S. & Plookphol, T. (2016) Load relaxation of olivine single crystals. *Journal of Geophysical Research: Solid Earth*. [Online] 121 (10), 7193–7210. Available from: doi:https://doi.org/10.1002/2016JB013425.

Crawford, O., Al-Attar, D., Tromp, J., Mitrovica, J.X., et al. (2018) Quantifying the sensitivity of post-glacial sea level change to laterally varying viscosity. *Geophysical Journal International*. [Online] 214 (2), 1324–1363. Available from: doi:10.1093/gji/ggy184.

Creveling, J.R., Mitrovica, J.X., Clark, P.U., Waelbroeck, C., et al. (2017) Predicted bounds on peak global mean sea level during marine isotope stages 5a and 5c. *Quaternary Science Reviews*. [Online] 163, 193–208. Available from: doi:10.1016/j.quascirev.2017.03.003.

Dickinson-Lovell, H., Huang, M.-H., Freed, A.M., Fielding, E., et al. (2018) Inferred rheological structure and mantle conditions from postseismic deformation following the 2010 Mw 7.2 El Mayor-Cucapah Earthquake. *Geophysical Journal International*. [Online] 213 (3), 1720–1730. Available from: doi:10.1093/gji/ggx546 [Accessed: 11 February 2020].

Dziewonski, A.M. (1981) Preliminary reference Earth model. *Physics of The Earth and Planetary Interiors*. [Online] 25 (4), 297–356. Available from: doi:10.1016/0031-9201(81)90046-7.

Farla, R.J.M., Jackson, I., Fitz Gerald, J.D., Faul, U.H., et al. (2012) Dislocation Damping and Anisotropic Seismic Wave Attenuation in Earth's Upper Mantle. *Science*. [Online] 336 (6079), 332 LP – 335. Available from: doi:10.1126/science.1218318.

Faul, U. & Jackson, I. (2015) Transient Creep and Strain Energy Dissipation: An Experimental Perspective. *Annual Review of Earth and Planetary Sciences*. [Online] 43 (1), 541–569. Available from: doi:10.1146/annurev-earth-060313-054732 [Accessed: 9 November 2017].

Fischer, K.M., Ford, H.A., Abt, D.L. & Rychert, C.A. (2010) The Lithosphere-Asthenosphere Boundary. *Annual Review of Earth and Planetary Sciences*. [Online] 38 (1), 551–575. Available from: doi:10.1146/annurev-earth-040809-152438.

Gomez, N., Mitrovica, J.X., Huybers, P. & Clark, P.U. (2010) Sea level as a stabilizing factor for marine-ice-sheet grounding lines. *Nature Geoscience*. [Online] 3 (12), 850–853. Available from: doi:10.1038/ngeo1012.

Gunasekaran, S. & Ak, M.M. (2002) *Cheese Rheology and Texture*. [Online]. CRC Press. Available from: https://books.google.com/books?id=KBzNBQAAQBAJ.

Hager, B.H., Clayton, R.W., Richards, M.A., Comer, R.P., et al. (1985) Lower mantle heterogeneity, dynamic topography and the geoid. *Nature*. [Online] 313, 541–545. Available from: http://adsabs.harvard.edu/abs/1984lmhd.rept.....H [Accessed: 18 March 2014].

Hansen, L.N., Zimmerman, M.E. & Kohlstedt, D.L. (2011) Grain boundary sliding in San Carlos olivine: Flow law parameters and crystallographic-preferred orientation. *Journal of Geophysical Research: Solid Earth*. [Online] 116 (8). Available from: doi:10.1029/2011JB008220.

Hansen, L.N., Wallis, D., Breithaupt, T., Thom, C.A., et al. (2020) Dislocation creep of olivine: Low-temperature plasticity controls transient creep at high temperatures. *Journal of Geophysical Research: Solid Earth*. (in review)

Havlin, C., Holtzman, B. & Hopper, E. (2020) Inference of thermodynamic state in the asthenosphere from anelastic properties, with applications to North American upper mantle. *Physics of the Earth and Planetary Interiors*. (in review)

Hirth, G. & Kohlstedt, D. (2004) Rheology of the upper mantle and the mantle wedge: A view from the experimentalists. In: *Geophysical Monograph Series*. [Online]. Blackwell Publishing Ltd. pp. 83–105. Available from: doi:10.1029/138GM06.

Hopper, E. & Fischer, K.M. (2018) The Changing Face of the Lithosphere-Asthenosphere Boundary: Imaging Continental Scale Patterns in Upper Mantle Structure Across the Contiguous U.S. With Sp Converted Waves. *Geochemistry, Geophysics, Geosystems*. [Online] 19 (8), 2593–2614. Available from: doi:10.1029/2018GC007476 [Accessed: 11 February 2020].

Huang, P., Wu, P. & Steffen, H. (2019) In search of an ice history that is consistent with composite rheology in Glacial Isostatic Adjustment modelling. *Earth and Planetary Science Letters*. [Online] 517, 26–37. Available from: doi:https://doi.org/10.1016/j.epsl.2019.04.011.

Ivins, E.R., Watkins, M.M., Yuan, D.N., Dietrich, R., et al. (2011) On-land ice loss and glacial isostatic adjustment at the Drake Passage: 2003-2009. *Journal of Geophysical Research: Solid Earth*. [Online] 116 (2). Available from: doi:10.1029/2010JB007607.

Ivins, E.R., Caron, L., Adhikari, S., Larour, E., et al. (2020) A linear viscoelasticity for decadal to centennial time scale mantle deformation. *Reports on Progress in Physics*. [Online] 83 (10), 106801. Available from: doi:10.1088/1361-6633/aba346.

Kanamori, H. & Anderson, D.L. (1977) Importance of physical dispersion in surface wave and free oscillation problems: Review. *Reviews of Geophysics*. [Online] 15 (1), 105. Available from: doi:10.1029/RG015i001p00105 [Accessed: 20 March 2014].

Lau, H.C.P., Austermann, J., Mitrovica, J.X., Crawford, O., et al. (2018) Inferences of Mantle Viscosity Based on Ice Age Data Sets: The Bias in Radial Viscosity Profiles Due to the Neglect of Laterally Heterogeneous Viscosity Structure. *Journal of Geophysical Research: Solid Earth*. [Online] 123 (9), 7237–7252. Available from: doi:https://doi.org/10.1029/2018JB015740.

Lau, H.C.P. & Faul, U.H. (2019) Anelasticity from seismic to tidal timescales: Theory and observations. *Earth and Planetary Science Letters*. [Online] 508, 18–29. Available from: doi:10.1016/j.epsl.2018.12.009.

Lau, H.C.P. & Holtzman, B.K. (2019) "Measures of Dissipation in Viscoelastic Media" Extended: Toward Continuous Characterization Across Very Broad Geophysical Time Scales. *Geophysical Research Letters*. [Online] 46 (16), 9544–9553. Available from: doi:10.1029/2019GL083529 [Accessed: 11 February 2020].

Lekić, V., Matas, J., Panning, M. & Romanowicz, B. (2009) Measurement and implications of frequency dependence of attenuation. *Earth and Planetary Science Letters*. [Online] 282 (1–4), 285–293. Available from: doi:10.1016/j.epsl.2009.03.030 [Accessed: 17 October 2017].

Liu, J., Milne, G.A., Kopp, R.E., Clark, P.U., et al. (2016) Sea-level constraints on the amplitude and source distribution of Meltwater Pulse 1A. *Nature Geoscience*. [Online] 9 (2), 130–134. Available from: doi:10.1038/ngeo2616.

Lloyd, A.J., Wiens, D.A., Zhu, H., Tromp, J., et al. (2020) Seismic Structure of the Antarctic Upper Mantle Based on Adjoint Tomography. *Journal of Geophysical Research: Solid Earth*. [Online] Available from: doi:10.1029/2019jb017823.

Mancinelli, N.J., Fischer, K.M. & Dalton, C.A. (2017) How Sharp Is the Cratonic Lithosphere-Asthenosphere Transition? *Geophysical Research Letters*. [Online] 44 (20), 10,110-189,197. Available from: doi:10.1002/2017GL074518.

McCarthy, C., Takei, Y. & Hiraga, T. (2011) Experimental study of attenuation and dispersion over a broad frequency range: 2. The universal scaling of polycrystalline materials. *Journal of Geophysical Research*. [Online] 116 (B9), B09207. Available from: doi:10.1029/2011JB008384 [Accessed: 15 May 2016].

Mitrovica, J.X. & Milne, G.A. (2003) On post-glacial sea level: I. General theory. *Geophysical Journal International*. [Online] 154 (2), 253–267. Available from: doi:10.1046/j.1365-246X.2003.01942.x [Accessed: 11 February 2020].

Nakada, M. & Lambeck, K. (1989) Late Pleistocene and Holocene sea-level change in the Australian region and mantle rheology. *Geophysical Journal International*. [Online] 96 (3), 497–517. Available from: doi:10.1111/j.1365-246X.1989.tb06010.x [Accessed: 11 February 2020].

Nield, G.A., Barletta, V.R., Bordoni, A., King, M.A., et al. (2014) Rapid bedrock uplift in the Antarctic Peninsula explained by viscoelastic response to recent ice unloading. *Earth and Planetary Science Letters*. [Online] 397, 32–41. Available from: doi:10.1016/j.epsl.2014.04.019.

Nowick, A.S. & Berry, B.S. (1972) *Anelastic relaxation in crystalline solids*. Academic Press.

Peltier, W.R. (2004) Global Glacial Isostasy and the Surface of the Ice-Age Earth: The ICE-5G (VM2) Model and GRACE. *Annual Review of Earth and Planetary Sciences*. [Online] 32 (1), 111–149. Available from: doi:10.1146/annurev.earth.32.082503.144359 [Accessed: 6 February 2015].

Pollitz, F.F., Peltzer, G. & Bürgmann, R. (2000) Mobility of continental mantle: Evidence from postseismic geodetic observations following the 1992 Landers earthquake. *Journal of Geophysical Research: Solid Earth*. [Online] 105 (B4), 8035–8054. Available from: doi:10.1029/1999jb900380.

Samrat, N.H., King, M.A., Watson, C., Hooper, A., et al. (2020) Reduced ice mass loss and three-dimensional viscoelastic deformation in northern Antarctic Peninsula inferred from

GPS. *Geophysical Journal International*. [Online] 222 (2), 1013–1022. Available from: doi:10.1093/gji/ggaa229.

Sella, G.F., Stein, S., Dixon, T.H., Craymer, M., et al. (2007) Observation of glacial isostatic adjustment in "stable" North America with GPS. *Geophysical Research Letters*. [Online] 34 (2), L02306. Available from: doi:10.1029/2006GL027081 [Accessed: 1 March 2014].

Shen, W. & Ritzwoller, M.H. (2016) Crustal and uppermost mantle structure beneath the United States. *Journal of Geophysical Research: Solid Earth*. [Online] 121 (6), 4306–4342. Available from: doi:10.1002/2016JB012887 [Accessed: 11 February 2020].

Shito, A., Karato, S. & Park, J. (2004) Frequency dependence of Q in Earth's upper mantle inferred from continuous spectra of body waves. *Geophysical Research Letters*. [Online] 31 (12), n/a-n/a. Available from: doi:10.1029/2004GL019582 [Accessed: 15 May 2016].

Stixrude, L. & Lithgow-Bertelloni, C. (2005) Thermodynamics of mantle minerals - I. Physical properties. *Geophysical Journal International*. [Online]. 162 (2) pp.610–632. Available from: doi:10.1111/j.1365-246X.2005.02642.x.

Sundberg, M. & Cooper, R.F. (2010) A composite viscoelastic model for incorporating grain boundary sliding and transient diffusion creep; correlating creep and attenuation responses for materials with a fine grain size. *Philosophical Magazine*. [Online] 90 (20), 2817–2840. Available from: doi:10.1080/14786431003746656 [Accessed: 8 November 2017].

Takei, Y. (2017) Effects of Partial Melting on Seismic Velocity and Attenuation: A New Insight from Experiments. *Annual Review of Earth and Planetary Sciences*. [Online] 45 (1), 447–470. Available from: doi:10.1146/annurev-earth-063016-015820 [Accessed: 11 February 2020].

Thieme, M., Demouchy, S., Mainprice, D., Barou, F., et al. (2018) Stress evolution and associated microstructure during transient creep of olivine at 1000–1200 °C. *Physics of the Earth and Planetary Interiors*. [Online] 278, 34–46. Available from: doi:https://doi.org/10.1016/j.pepi.2018.03.002.

van der Wal, W., Barnhoorn, A., Stocchi, P., Gradmann, S., et al. (2013) Glacial isostatic adjustment model with composite 3-D Earth rheology for Fennoscandia. *Geophysical Journal International*. [Online] 194 (1), 61–77. Available from: doi:10.1093/gji/ggt099 [Accessed: 12 September 2017].

van der Wal, W., Whitehouse, P.L. & Schrama, E.J.O. (2015) Effect of GIA models with 3D composite mantle viscosity on GRACE mass balance estimates for Antarctica. *Earth and Planetary Science Letters*. [Online] 414, 134–143. Available from: doi:10.1016/j.epsl.2015.01.001 [Accessed: 12 September 2017].

Watts, A.B., Zhong, S.J. & Hunter, J. (2013) The Behavior of the Lithosphere on Seismic to Geologic Timescales. *Annual Review of Earth and Planetary Sciences*. [Online] 41 (1), 443–468. Available from: doi:10.1146/annurev-earth-042711-105457 [Accessed: 11 February 2020].

Wolstencroft, M., King, M.A., Whitehouse, P.L., Bentley, M.J., et al. (2015) Uplift rates from a new high-density GPS network in Palmer Land indicate significant late Holocene ice loss in the southwestern Weddell Sea. *Geophysical Journal International*. [Online] 203 (1), 737–754. Available from: doi:10.1093/gji/ggv327.

Wu, P. & Peltier, W.R. (1982) Viscous gravitational relaxation. *Geophysical Journal International*. [Online] 70 (2), 435–485. Available from: doi:10.1111/j.1365-246X.1982.tb04976.x [Accessed: 29 April 2015].

Yamauchi, H. & Takei, Y. (2016) Polycrystal anelasticity at near-solidus temperatures. *Journal of Geophysical Research: Solid Earth*. [Online] 121 (11), 7790–7820. Available from: doi:https://doi.org/10.1002/2016JB013316.

Yokoyama, Y., Lambeck, K., De Deckker, P., Johnston, P., et al. (2000) Timing of the Last Glacial Maximum from observed sea-level minima. *Nature*. [Online] 406 (6797), 713–716. Available from: doi:10.1038/35021035.

Yuen, D.A., Sabadini, R.C.A., Gasperini, P. & Boschi, E. (1986) On transient rheology and glacial isostasy. *Journal of Geophysical Research*. [Online] 91 (B11), 11420. Available from: doi:10.1029/JB091iB11p11420 [Accessed: 11 February 2020].

Zhong, S., Paulson, A. & Wahr, J. (2003) Three-dimensional finite-element modelling of Earth's viscoelastic deformation: effects of lateral variations in lithospheric thickness. *Geophysical Journal International*. [Online] 155 (2), 679–695. Available from: doi:10.1046/j.1365-246X.2003.02084.x [Accessed: 11 March 2016].

Figure 1. Estimates and locations of plate thickness and upper mantle viscosity. A compilation of **(a)** lithospheric/plate thickness, z_{LAB}, and **(b)** upper mantle viscosity, η, across Western North America, W-NA (Creveling et al., 2017; Austermann et al., 2020; Dicinson-Lovell et al., 2018; Pollitz et al., 2000; Hopper and Fischer, 2018) , Western Antarctica, W-ANT (Barletta et al., 2018; [An et al., 2015), and the Antarctic Peninsula, ANT-P (Wolstencroft et al., 2015; Ivins et al., 2011; Nield et al., 2014; Samrat et al., 2020; An et al., 2015). These estimates are derived from seismic, post-seismic relaxation, lake rebound, and GIA data. **(c,d)** Approximate locations of the observation-driven estimates and the tomographic models used in Section 2.2.1, where panels **(c)** and **(d)** show models at depths of 150 km of Shen & Ritzwoller (2016) and Lloyd et al. (2020), respectively.

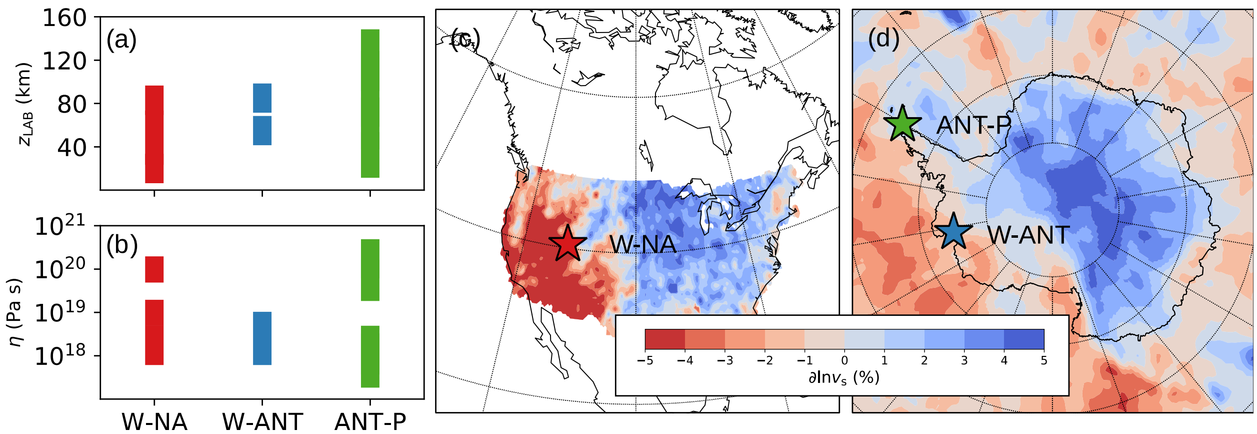

Figure 2. Phenomenological Viscoelastic Models.
Depiction of 1-D phenomenological viscoelastic models. The dark gray circle symbolically represents any combination of springs and dashpots that mimic transient deformation. Replacing the circle with any of the components linked by an arrow will form the commonly adopted models labelled. With the addition of steady state dislocation creep, the viscosity of the steady state dashpot, η_0, becomes stress, σ, dependent.

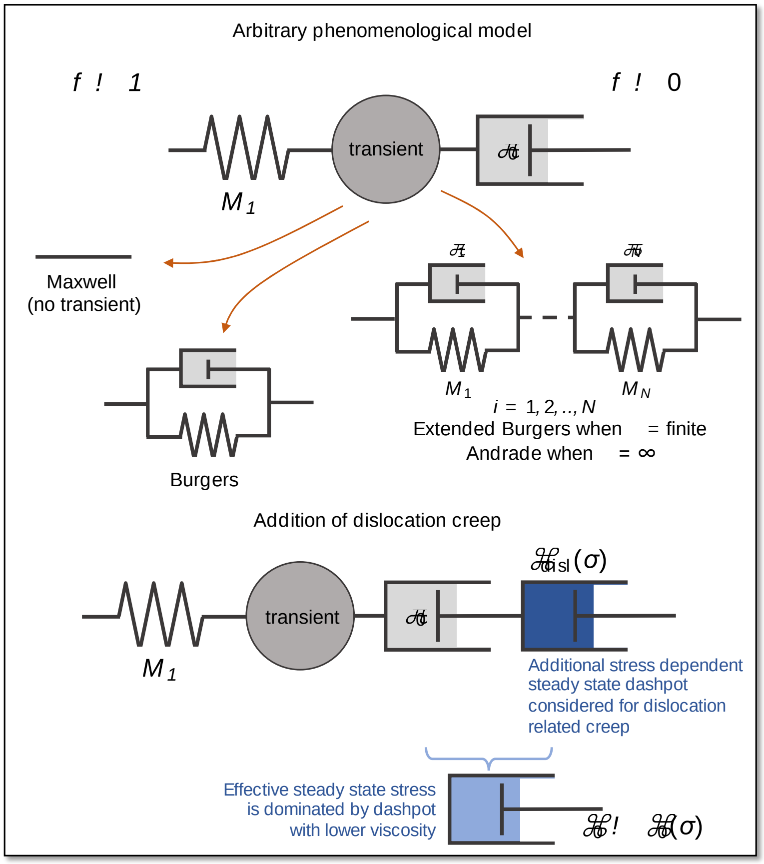

Figure 3. Mapping out dissipation parameters with geophysical observations
(a) A schematic depiction of seismic wave-speed reduction (top panel) at lower frequencies due to dispersion (or $\mathrm{Re}[M^*(\omega)]$) and the increase of attenuation, $Q^{-1}(\omega)$ (bottom panel) at lower frequencies. The boxes denote how these trends are sampled by seismic data at different frequencies. **(b)** The analog to **(a)** but how GIA processes may sample apparent viscosity, $\tilde{\eta}(\omega)$.

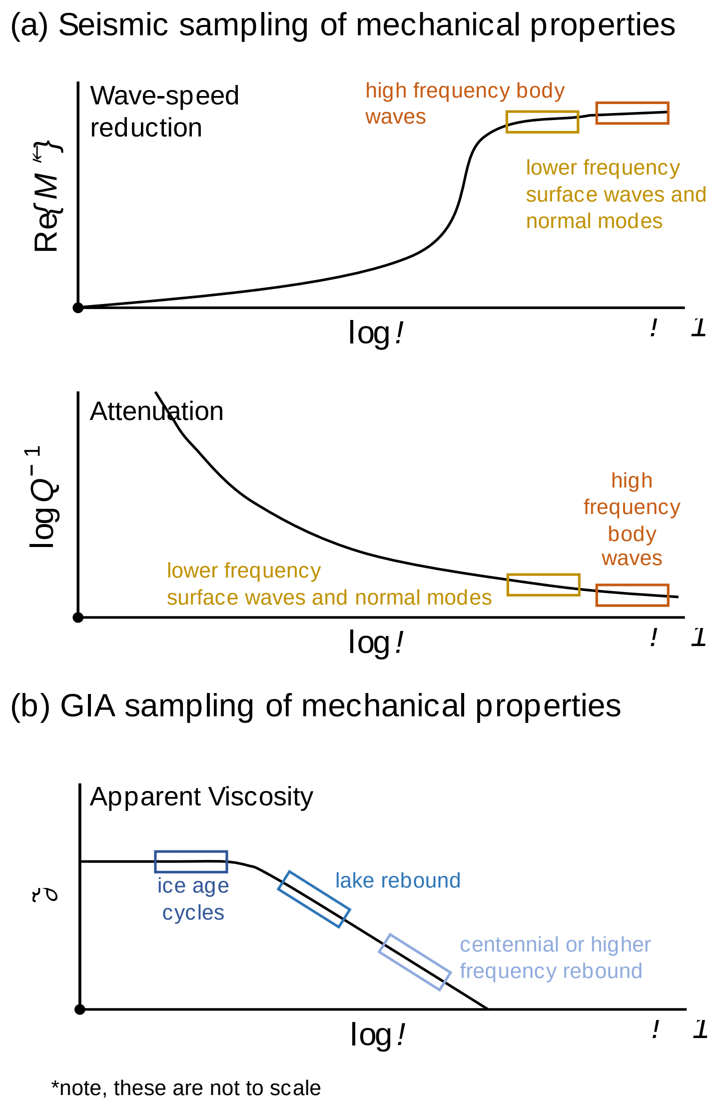

Figure 4. Methodology for determining viscoelastic structure.
Schematic flowchart depicting the main steps in producing full spectrum viscoelastic structure at each case region (Section 2.2.1).

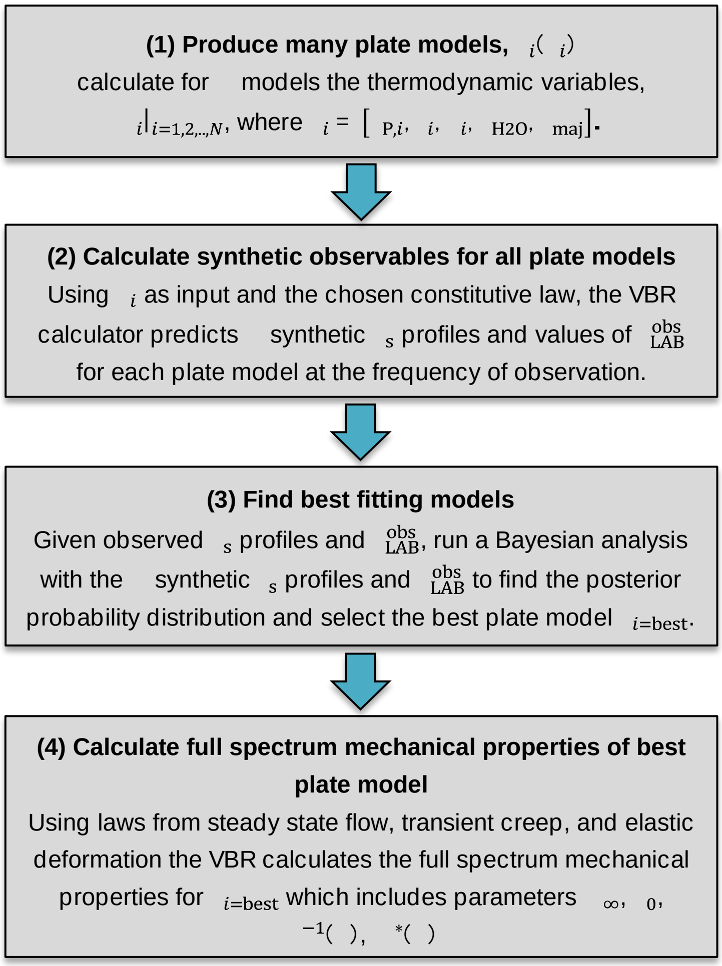

Figure 5. Resulting Thermodynamic and Mechanical Properties of Case Regions. For each region **(a)**, **(b)**, **(c)**, subpanel **(i)** shows the shear wave-speed, v_S, profiles at select regions in Fig. 1(c,d) (averaged over a lateral radius of 50 km) from the tomographic models of Shen & Ritzwoller (2016) **(a)** and Lloyd et al. (2020) **(b,c)**. The orange shaded region marks the depth window across which we used the v_S data to constrain the sub-lithospheric temperature profile, where the circles mark the resulting averaged v_S to be fit. Subpanels **(ii-v)** are generated by the VBR fitting procedure (see Fig. 4 and Section 2.2.1), where **(ii)** shows the resulting best fit v_S while **(iii)** shows the associated temperature profile (solid black line). The following corresponding mechanical properties are, in subpanel **(iii)** the steady state viscosity η_0, where the horizontal lines mark the base of the lithosphere; **(iv)** the apparent plate thickness, $\tilde{z}_{LAB}$, and **(v)** the apparent asthenospheric viscosity $\tilde{\eta}_{AST}$, as a function of frequency, f. Subpanels **(iv-v)** have been averaged in depth across the asthenosphere and the shaded regions mark the effect of including steady state dislocation creep across a stress range ($0 \leq \sigma \leq 10$ MPa). The colored solid and gray lines coincide with σ = 0 MPa and σ = 1 MPa, respectively. Within subpanels **(iv-v)**, we have placed the observationally derived estimates (boxes) from Fig. 1 where appropriate. The vertical gray shaded region spans the seismic band (within which we constrained the thermodynamic conditions) for comparison.

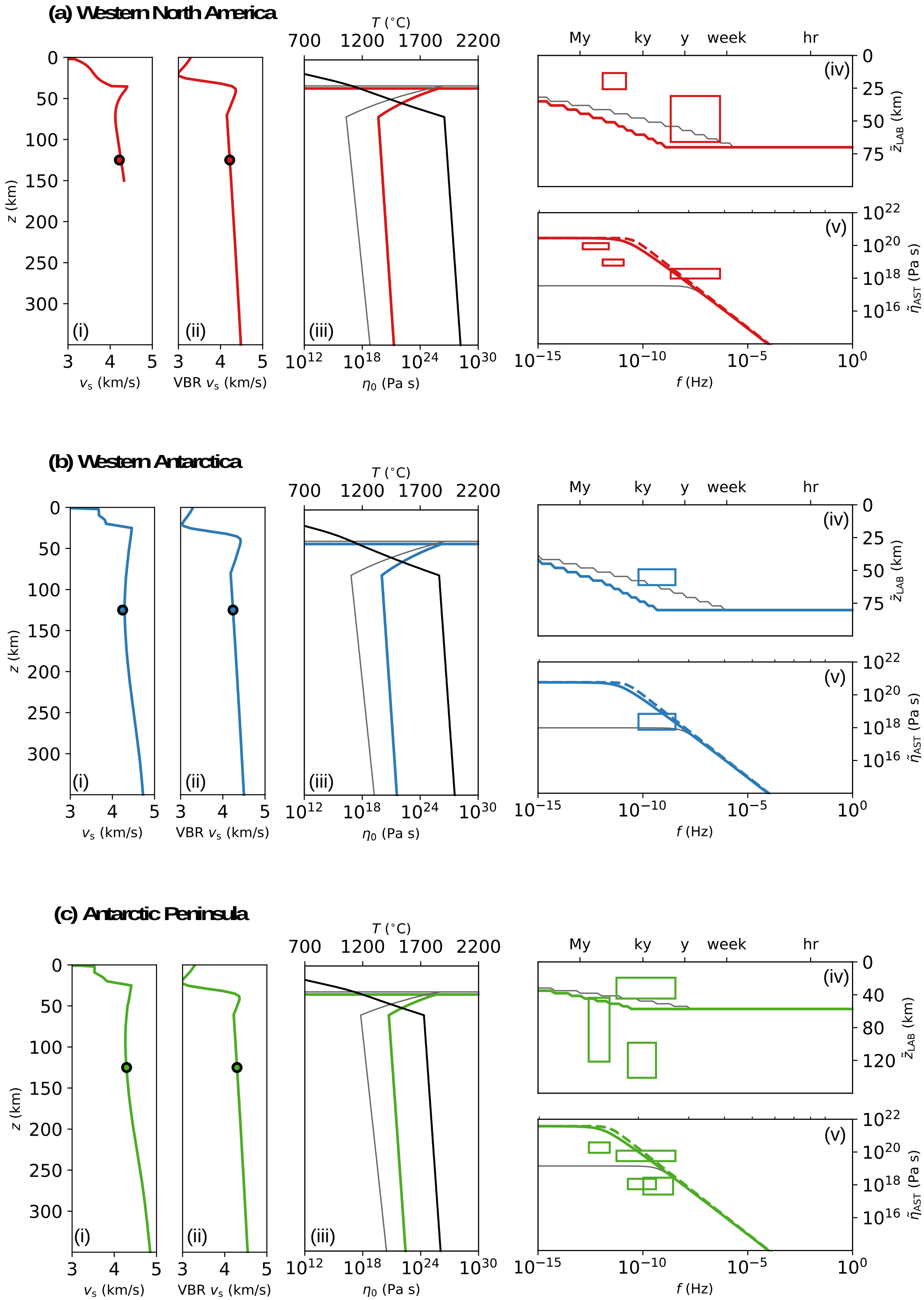
(a) Western North America
(b) Western Antarctica
(c) Antarctic Peninsula
z (km)
vs (km/s)
VBR vs (km/s)
T (°C)
η0 (Pa s)
f (Hz)
My
ky
y
week
hr
z̃LAB (km)
η̃AST (Pa s)
(i)
(ii)
(iii)
(iv)
(v)

Figure 6. Converting time domain observations to the frequency domain
(a) Schematic depiction of applied stress history, $\sigma(t)$, labelling the two relevant timescales, τ_{dur} and τ_{del}. **(b)** The apparent viscosities for each region of the 1-D Andrade model that $\sigma(t)$ is applied to. The solid lines are reproduced from Fig. 5 (subpanels iii) and circles are the result of finding the best fitting Andrade parameters for each region. **(c-e)** For a given τ_{dur} and τ_{del} pair, the contours mark the frequency for which the estimated $\tilde{\eta}^*_{\mathrm{est}}$ (assuming a Maxwell model) is equivalent to $\tilde{\eta}^*_{\mathrm{An}}$ (i.e., where $\tilde{\eta}^*_{\mathrm{est}} = \tilde{\eta}^*_{\mathrm{An}}(f_{\mathrm{An}})$). The boxes are the associated ranges for each observation we include (see Fig. 1).